

## Article

# The Possibility of Layered Non-Van Der Waals Boron Group Oxides: A First-Principles Perspective

Yu Zhou <sup>1</sup>, Jun Zhu <sup>2</sup>, Dongyu Cai <sup>1,\*</sup> and Yingchun Cheng <sup>1,\*</sup>

<sup>1</sup> Key Laboratory of Flexible Electronics & Institute of Advanced Materials, Jiangsu National Synergetic Innovation Center for Advanced Materials, Nanjing Tech University, 30 South Puzhu Road, Nanjing 211816, China; iamyuzhou@njtech.edu.cn

<sup>2</sup> College of Physics Science and Technology, Yangzhou University, Yangzhou 225002, China; zhujun@yzu.edu.cn

\* Correspondence: iamdycai@njtech.edu.cn (D.C.); iamyccheng@njtech.edu.cn (Y.C.)

**Abstract:** Two-dimensional (2D) metal oxides have broad prospective applications in the fields of catalysis, electronic devices, sensors, and detectors. However, non-van der Waals 2D metal oxides have rarely been studied because they are hard to peel off or synthesize. In this work, taking alumina ( $\text{Al}_2\text{O}_3$ ) as a typical representative of 2D boron group oxides, the structural stability and electrical properties of 2D  $\text{Al}_2\text{O}_3$  are investigated through first-principles calculations. The thinnest  $\text{Al}_2\text{O}_3$  structure is a bilayer, and the band gap of  $\text{Al}_2\text{O}_3$  is found to decrease with decreasing layer thickness because of the giant surface reconstruction. The band gap of bilayer  $\text{X}_2\text{O}_3$  ( $\text{X} = \text{Al}, \text{Ga}, \text{and In}$ ) decreases with increasing atomic radius. Our findings provide theoretical support for the preparation of non-van der Waals 2D boron group oxide semiconductors.

**Keywords:** boron group oxides; non-van der Waals material; first-principles calculation



**Citation:** Zhou, Y.; Zhu, J.; Cai, D.; Cheng, Y. The Possibility of Layered Non-Van Der Waals Boron Group Oxides: A First-Principles Perspective. *Crystals* **2023**, *13*, 1298. <https://doi.org/10.3390/cryst13091298>

Academic Editor: Thorsten Hesjedal

Received: 24 July 2023

Revised: 19 August 2023

Accepted: 22 August 2023

Published: 23 August 2023



**Copyright:** © 2023 by the authors. Licensee MDPI, Basel, Switzerland. This article is an open access article distributed under the terms and conditions of the Creative Commons Attribution (CC BY) license (<https://creativecommons.org/licenses/by/4.0/>).

## 1. Introduction

Since the discovery of graphene in 2004 [1], two-dimensional (2D) materials have been receiving increasing attention because of their excellent thermal, mechanical, optical, and electrical properties. Besides graphene, other 2D materials, such as black phosphorus, covalent organic frameworks, hexagonal boron nitride, layered double hydroxides, metals, metal oxides, metal–organic frameworks, transition metal carbides/nitrides (MXenes), and transition metal dichalcogenides [2–4], have been discovered and investigated extensively. Because metal oxides are abundant in nature, 2D metal oxides are expected to integrate with other 2D materials for electronic, spintronic, and optoelectronic applications [5–11]. Although some van der Waals (vdW) layered metal oxides, such as  $\text{SnO}$  and  $\text{PbO}$  [12,13], have been predicted, the corresponding experimental realization of vdW layered metal oxides is sparse [14]. Therefore, many attempts have recently been made to prepare non-vdW layered metal oxides, such as  $\text{WO}_3$  and  $\text{MoO}_3$  [15–19]. Non-vdW metal oxides are difficult to exfoliate into a few layers due to their strong chemical bonds in three dimensions, and the bottom-up synthesis method also poses significant difficulties and challenges [20]. As a result, less has been reported on 2D non-vdW metal oxides, and their corresponding properties have not been fully explored.

Binary non-vdW boron group oxides, such as  $\text{Al}_2\text{O}_3$ ,  $\text{Ga}_2\text{O}_3$ , and  $\text{In}_2\text{O}_3$ , are wide-band-gap semiconductors and have been applied in electronic devices and photodetectors [21,22]. Because of its ultra-wide band gap and good thermal conductivity,  $\text{Al}_2\text{O}_3$  is often used in ceramic applications [23–25]. A bottom-up method to synthesize graphene-like  $\gamma\text{-Al}_2\text{O}_3$  nanosheets has been reported [26]. Using graphene oxide (GO) as template, a homogeneous aluminum sulfate layer was firstly deposited on the GO sheets. Then, the prepared GO–Al composite sheets were calcined to remove GO and convert basic aluminum sulfate into  $\gamma\text{-Al}_2\text{O}_3$  nanosheets [26]. The  $\gamma\text{-Al}_2\text{O}_3$  nanosheets exhibit faster adsorption kinetics

and larger adsorption capacity, which suggests broad applications in catalysis and environmental science. However, the metastable  $\gamma$ -Al<sub>2</sub>O<sub>3</sub> will transform into stable  $\alpha$ -Al<sub>2</sub>O<sub>3</sub> under higher temperature. Theoretically, various different monolayer aluminum oxide have been predicted [27–29], for example, hexagonal Al<sub>2</sub>O<sub>3</sub> [29] and rectangle AlO<sub>2</sub> [27]. Therefore, exploring the stability of 2D  $\alpha$ -Al<sub>2</sub>O<sub>3</sub> is highly essential. Ga<sub>2</sub>O<sub>3</sub> is a transparent semiconductor with wide band gap and high critical electric field, and therefore holds the promising applications in power electronics and solar blind photodetectors [30–34]. In<sub>2</sub>O<sub>3</sub> doped by Sn has been widely used for electronic and optoelectronic devices, such as solar cell [35], optical window [36], film transistor [37], and Schottky contact [38]. Because of its ultra-flat surface, Al<sub>2</sub>O<sub>3</sub> (0001) substrate is considered a promising substrate for 2D materials, such as graphene and transition metal dichalcogenides obtained by chemical vapor deposition [39–42]. Recently, Ga<sub>2</sub>O<sub>3</sub> is also applied as a substrate to grow transition metal dichalcogenides nanoribbons. Because of their similar structures, 2D Al<sub>2</sub>O<sub>3</sub>, Ga<sub>2</sub>O<sub>3</sub>, and In<sub>2</sub>O<sub>3</sub> are promising when coupled with 2D electronic devices. It has been reported that 2D Fe<sub>2</sub>O<sub>3</sub> was successfully synthesized via the liquid-phase exfoliation of hematite ore in an organic solvent N,N-dimethylformamide (DMF) [43]. Because bulk Fe<sub>2</sub>O<sub>3</sub> has a similar structure to boron group oxides, the synthesis of other non-van der Waals 2D metal oxide materials should thus also be achievable.

In this work, taking 2D Al<sub>2</sub>O<sub>3</sub> as a representative, we design a series of stable 2D boron group oxides using first-principles calculations and investigate their crystal structures, stability, and electronic structures. Two-dimensional Al<sub>2</sub>O<sub>3</sub> is stable down to the bilayer limit and the band gap of few-layer Al<sub>2</sub>O<sub>3</sub> increases with increasing layer thickness. This is the opposite of the band gap thickness trend of vdW layered materials, such as black phosphorus and transition metal dichalcogenides. In addition, we investigate the stability and electronic properties of bilayer Ga<sub>2</sub>O<sub>3</sub> and In<sub>2</sub>O<sub>3</sub>, assuming both bilayers are thermally stable. Our work predicts promising stability for 2D non-vdW boron group oxides and provides theoretical support for the future experimental preparation of 2D boron group oxides.

## 2. Methods

All first-principles calculations in this work, such as structural optimization, phonon dispersion, and electronic properties of Al<sub>2</sub>O<sub>3</sub> with different number of layers, were performed using the QUANTUM ESPRESSO package based on density functional theory (DFT) [44,45]. The Perdew–Burke–Ernzerhof (PBE) functional of the generalized gradient approximation (GGA) was adopted for electron exchange and correlation interactions [46]. Ultrasoft pseudopotentials were selected to describe the interaction between electrons and ions. A vacuum spacing of 20 Å was used to minimize the interaction between neighboring slabs. The cut-off energy of 680 eV and the Brillouin zone sampling of a 10 × 10 × 1 Monkhorst–Pack k-point grid [47] were applied for all layered structures. The convergence threshold for self-consistency was set as 10<sup>−11</sup> eV. To ensure the accuracy of the calculation, the structural optimization was continued until the residual forces converged to less than 1.4 × 10<sup>−3</sup> eV/Å and the total energy to less than 1.4 × 10<sup>−4</sup> eV. The phonon dispersions and Raman spectra were calculated using Phonon code within density-functional perturbation theory [48]. We used norm-conserving pseudopotentials (NCPPs) within the local density approximation (LDA) with a plane-wave cutoff energy of 816 eV to describe the interaction between electrons and ions. A 16 × 16 × 1 Monkhorst–Pack k-mesh and a 8 × 8 × 1 Monkhorst–Pack q-mesh were applied for the phonon dispersion calculations. For the Raman spectra calculations, a 10 × 10 × 1 Monkhorst–Pack k-mesh was used. The threshold for self-consistency was set at 1.36 × 10<sup>−13</sup> eV.

## 3. Results and Discussions

Pristine bulk Al<sub>2</sub>O<sub>3</sub> is trigonal with the space group R $\bar{3}c$  (Figure 1a). O<sup>2−</sup> ions are arranged in a hexagonal close packing and Al<sup>3+</sup> ions are filled into the octahedral voids. The calculated band gap of bulk Al<sub>2</sub>O<sub>3</sub> is 5.83 eV, which is close to the previously calculated

value (6.05 eV) [49]. To model the  $\text{Al}_2\text{O}_3$  (0001) surface, we consider the two common surface structures shown in Table 1. The thermodynamic stability of different surface structures can be evaluated based on the surface formation energy, which is defined by the following equation:  $E_f = E_{\text{surface}} - E_{\text{bulk}}$ , where  $E_{\text{surface}}$  is the energy of an optimized surface structure and  $E_{\text{bulk}}$  is the energy of optimized bulk  $\text{Al}_2\text{O}_3$ . The calculated surface formation energies of type I and II surfaces are listed in Table 1. The calculated surface formation energy of the type I surface is about 3.78 eV, which is a quarter of that of the type II surface. Therefore, the type I surface structure is more stable than the type II surface. In the following, all calculations are performed based on the type I surface structure.

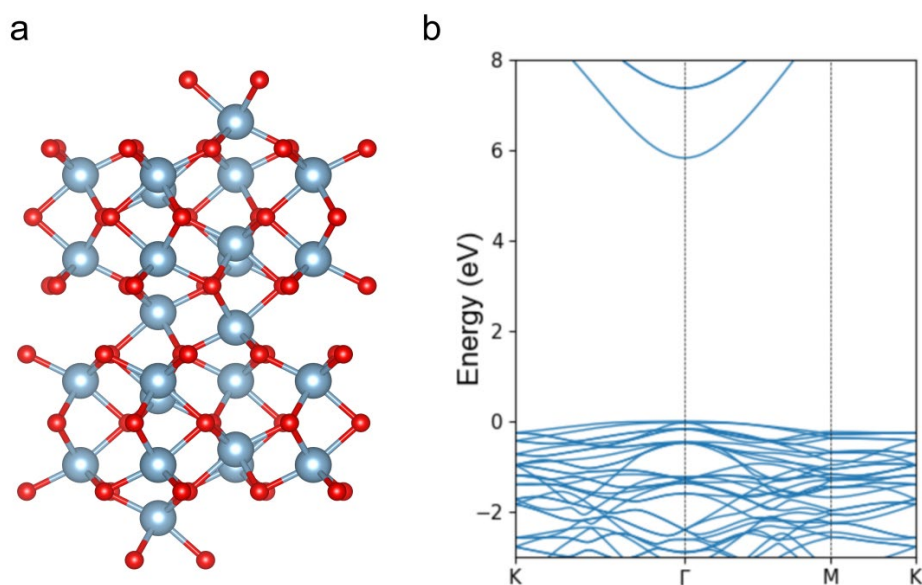


**Figure 1.** (a) Side view of the structure and (b) calculated electronic band structure for bulk  $\text{Al}_2\text{O}_3$ . The Fermi level is set at valence band maximum (VBM).

**Table 1.** The side views and  $E_f$  (eV) for type I and II  $\text{Al}_2\text{O}_3$ (0001) surface before and after optimization.

	Before Optimization	After Optimization	$E_f$ (eV)
Type I			3.78
Type II			15.12

The energetically stable structures of the monolayer, bilayer, trilayer, four-layer, and five-layer  $\text{Al}_2\text{O}_3$  are shown in Figure 2a–e. There are five atoms (two Al atoms and three O atoms) in the unit cell of monolayer  $\text{Al}_2\text{O}_3$ . By analogy, the bilayer, trilayer, four-layer, and five-layer  $\text{Al}_2\text{O}_3$  have 10, 15, 20, and 25 atoms, respectively. During the structural optimization, the Al atoms on the upper and lower surfaces gradually move inward, inducing a flat surface structure. The reconstruction of the surface may further enhance the stability of 2D  $\text{Al}_2\text{O}_3$ . Figure 2f shows the in-plane lattice constants of few-layer and

bulk  $\text{Al}_2\text{O}_3$ . The in-plane lattice constant for monolayer  $\text{Al}_2\text{O}_3$  is 5.84 Å, which is 21% larger than that of bulk  $\text{Al}_2\text{O}_3$  (4.81 Å). The large change in the lattice constants suggests that the monolayer  $\text{Al}_2\text{O}_3$  may be unstable. In addition, the lattices of the bilayer, trilayer, four-layer, and five-layer  $\text{Al}_2\text{O}_3$  are similar to that of bulk  $\text{Al}_2\text{O}_3$ , indicating that bilayer  $\text{Al}_2\text{O}_3$  is the thinnest  $\text{Al}_2\text{O}_3$  structure that can be fabricated experimentally.

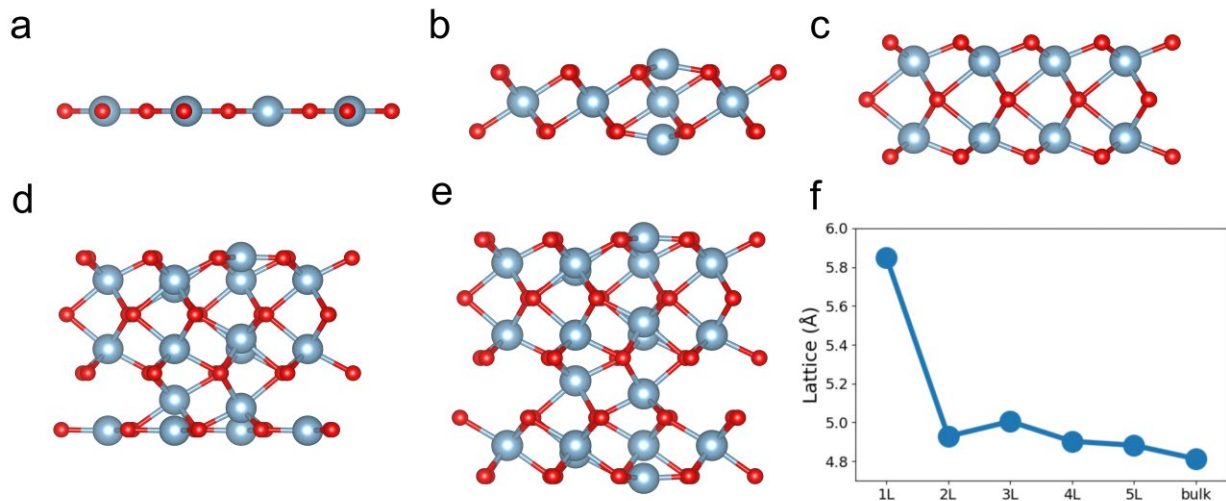


**Figure 2.** A side view of the optimized structures for the (a) monolayer, (b) bilayer, (c) trilayer, (d) four-layer, and (e) five-layer  $\text{Al}_2\text{O}_3$ . The gray and red balls represent Al and O atoms, respectively. (f) The optimized in-plane lattices of the few-layer and bulk  $\text{Al}_2\text{O}_3$ .

The dynamic stability of few-layer  $\text{Al}_2\text{O}_3$  can be examined from the phonon dispersions. The absence of negative frequencies in Figure 3a,b indicates that the monolayer and bilayer  $\text{Al}_2\text{O}_3$  are dynamically stable and can exist as free-standing 2D structures. Although monolayer  $\text{Al}_2\text{O}_3$  is dynamically stable, the giant lattice difference between monolayer and bulk  $\text{Al}_2\text{O}_3$  indicates the difficulty of synthesis monolayer  $\text{Al}_2\text{O}_3$  by top-down strategy. Considering the small lattice constant change and high dynamic stability of bilayer  $\text{Al}_2\text{O}_3$ , it can be inferred that the synthesis of bilayer  $\text{Al}_2\text{O}_3$  is quite possible by top-down or bottom-up method. Because of the large number of atoms in the cell of trilayer, four-layer, and five-layer  $\text{Al}_2\text{O}_3$ , the phonon calculation for these structures are extremely heavy. Here, the phonon dispersions of trilayer, four-layer, and five-layer  $\text{Al}_2\text{O}_3$  are not present. The in-plane lattice constants of trilayer, four-layer, and five-layer  $\text{Al}_2\text{O}_3$  are close to that of bilayer  $\text{Al}_2\text{O}_3$ , and we claim that the trilayer, four-layer, and five-layer  $\text{Al}_2\text{O}_3$  are likely synthesized experimentally.

Figure 4a–e show the electronic band structures of few-layer  $\text{Al}_2\text{O}_3$  calculated via the GGA scheme. The band gaps of the monolayer and five-layer  $\text{Al}_2\text{O}_3$  are direct, with the conduction band minimum (CBM) and the valence band maximum (VBM) located at the  $\Gamma$  point. The band gaps of bilayer, trilayer, and four-layer  $\text{Al}_2\text{O}_3$  are indirect, with the CBM located at the  $\Gamma$  point and the VBM located at a general point along the  $\Gamma$ –M line. In addition, with the increase in the number of layers, the band structure of  $\text{Al}_2\text{O}_3$  gradually shows the characteristics of a flat band in the VBM, which implies a large intensity of the density of states. Moreover, such a flat band in the VBM also indicates the large mass of hole carrier, which limits the mobility of holes.

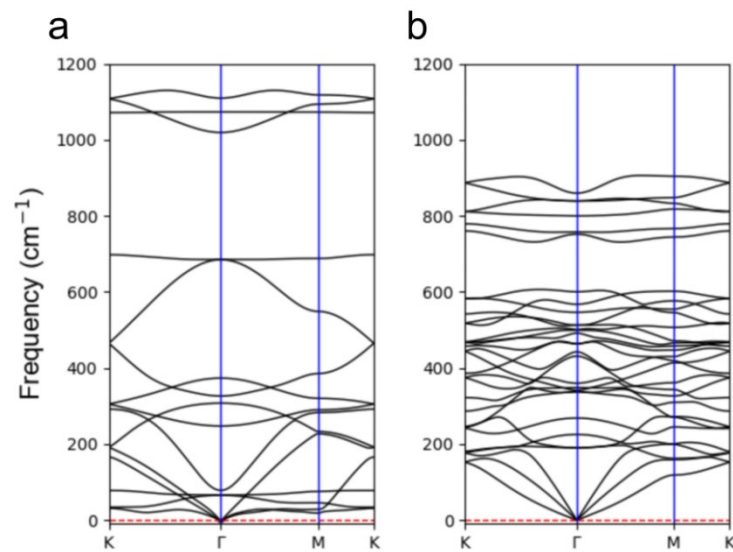


**Figure 3.** Phonon dispersions of (a) monolayer and (b) bilayer  $\text{Al}_2\text{O}_3$ .

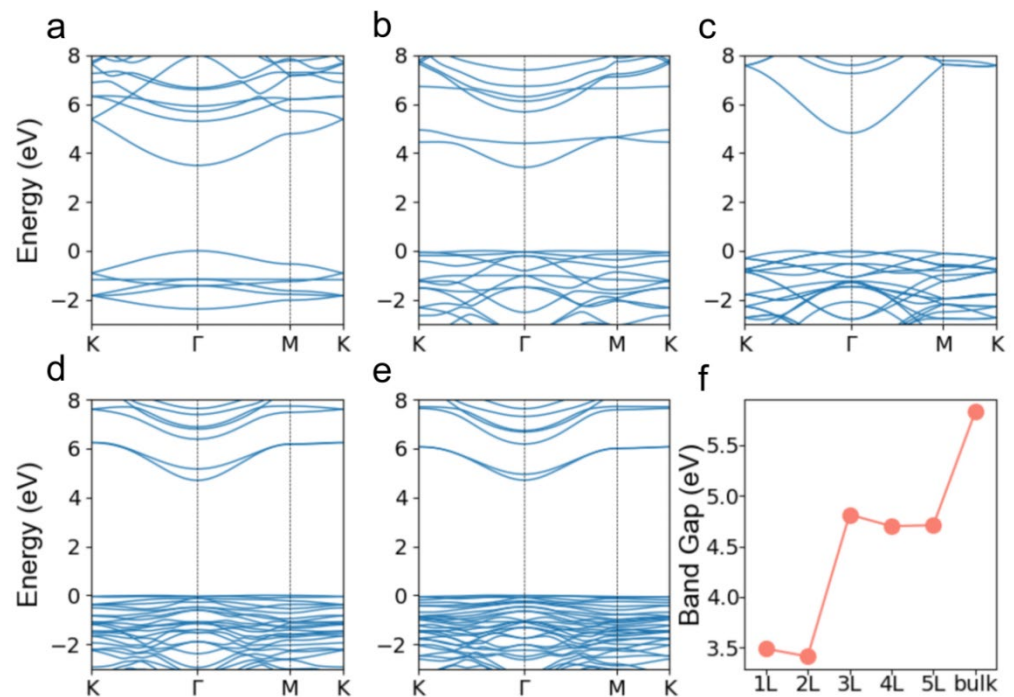


**Figure 4.** Band structures of (a) monolayer, (b) bilayer, (c) trilayer, (d) four-layer, and (e) five-layer  $\text{Al}_2\text{O}_3$ , respectively. The Fermi level is set at the valence band maximum (VBM). (f) The bandgap of few-layer and bulk  $\text{Al}_2\text{O}_3$ .

Figure 4f shows that the band gap of  $\text{Al}_2\text{O}_3$  increases with an increase in the number of layers. For comparison, the band structure of bulk  $\text{Al}_2\text{O}_3$  is presented in Figure 1b and shows a direct band gap of 5.83 eV. The values of the band gap for monolayer and bilayer  $\text{Al}_2\text{O}_3$  are similar ( $\sim 3.5$  eV), and those for the trilayer, four-layer, and five-layer  $\text{Al}_2\text{O}_3$  are also similar ( $\sim 4.7$  eV). It is well known that the band gap is always underestimated and lattice constants are overestimated when using GGA calculation due to the lack of Fock exchange. The hybrid functional will improve band gap and lattice constants because of including the exact exchange correction, but will induce a rise in computational costs [50,51]. In order to obtain the more reliable band gaps, we used the HSE06 hybrid functionals to calculate the band structures of monolayer and bilayer  $\text{Al}_2\text{O}_3$ , as shown in Figure 5. The band gaps are 5.08 and 4.95 eV for monolayer and bilayer  $\text{Al}_2\text{O}_3$ , respectively. The band

gap calculated through using HSE06 hybrid functional is about 1.5 eV larger than that through GGA. However, the band gap of bilayer  $\text{Al}_2\text{O}_3$  is also slightly smaller than that of monolayer  $\text{Al}_2\text{O}_3$  through using HSE06 hybrid functional, which is consistent with the results through GGA calculation. In addition, the band gap of monolayer  $\text{Al}_2\text{O}_3$  is direct, and that of bilayer  $\text{Al}_2\text{O}_3$  is indirect when using HSE06 functional, which is also consistent with the result obtained via GGA calculation. Therefore, the band gap calculated using the HSE06 hybrid functional is 1.5 eV larger than that through GGA, but the band gap nature and band gap variation on layer thickness are independent on the functional used. The band gaps of few-layer  $\text{Al}_2\text{O}_3$  are wider than 3.0 eV, corresponding to the ultraviolet spectral range. Therefore, the few-layer  $\text{Al}_2\text{O}_3$  is suitable for ultraviolet optoelectronic applications. The quantum confinement effect for most semiconductors means that the band gap increases as the thickness decreases. However, for  $\text{Al}_2\text{O}_3$ , the band gap narrows as the thickness decreases, indicating that the band gap variation with thickness cannot be explained by the quantum confinement effect. From the partial density of the states of on-surface and interior Al atoms for bilayer  $\text{Al}_2\text{O}_3$  (Figure 6), we can find that band edge states, which determine the band gap, mainly originate from on-surface Al atoms. Due to the surface states, the band gap of few-layer  $\text{Al}_2\text{O}_3$  is smaller than that of bulk  $\text{Al}_2\text{O}_3$  (Figure 4f). Because the surface reconstruction of few-layer  $\text{Al}_2\text{O}_3$  varies with thickness (Figure 2a–e), the band gap changes with thickness accordingly. Therefore, we attribute the band gap variation with the thickness to the different giant surface reconstruction of the few-layer  $\text{Al}_2\text{O}_3$ .

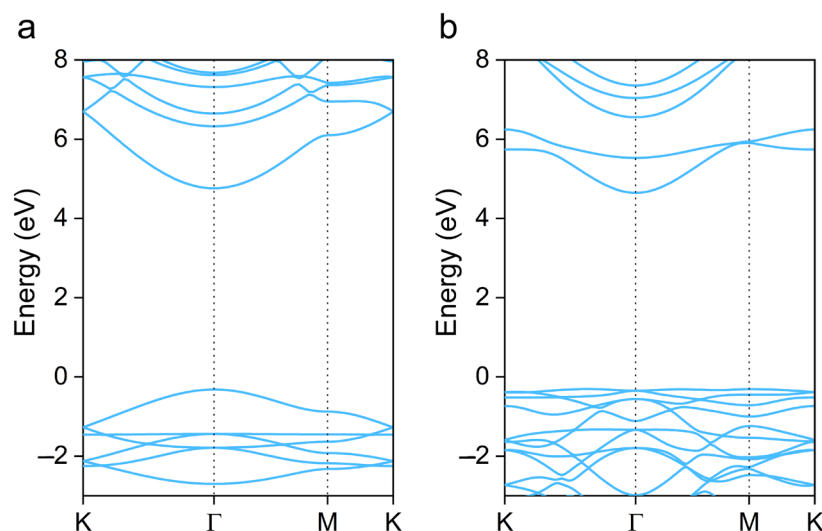


**Figure 5.** Band structures of (a) monolayer and (b) bilayer  $\text{Al}_2\text{O}_3$  using HSE06 hybrid functional.

Raman spectrum is an effective method with which to identify different materials and structures. In order to facilitate future experimental efforts on few-layer  $\text{Al}_2\text{O}_3$ , the Raman spectra of monolayer and bilayer  $\text{Al}_2\text{O}_3$  were calculated (see Figure 7). Monolayer  $\text{Al}_2\text{O}_3$  belongs to the space group  $P\bar{6}2m$  with 1 f.u. in the primitive cell (five atoms). The zone-center optical phonons can be classified as the following irreducible representations:  $\Gamma_{\text{opt}} = E'' + 3E' + A''1 + A'_1 + A''2 + A'_2$ , where  $E''$ ,  $E'$ , and  $A'_1$  are Raman active. For monolayer  $\text{Al}_2\text{O}_3$ , the peaks are centered at 387, 754, and 1043  $\text{cm}^{-1}$ , corresponding to the  $A'_1$ ,  $E'^{(1)}$ , and  $E'^{(2)}$  modes, respectively. The corresponding vibration for  $A'_1$ ,  $E'^{(1)}$ , and  $E'^{(2)}$  modes are listed in Table 2. In addition, in Figure 7a, the intensity of  $A'_1$  at 387  $\text{cm}^{-1}$  is significantly higher than the other two peaks. Therefore, the  $A'_1$  mode can be used as a Raman signature of monolayer  $\text{Al}_2\text{O}_3$ . Bilayer  $\text{Al}_2\text{O}_3$  belongs to the space group  $P\bar{3}1m$  with 2 f.u. (10 atoms) in the primitive cell. Therefore, bilayer  $\text{Al}_2\text{O}_3$  has 30 vibrational modes. Among these modes, five  $E_g$  and three  $A_{1g}$  modes are Raman active. For bilayer  $\text{Al}_2\text{O}_3$ , there are five dominant modes at 367, 521, 554, 797, and 881  $\text{cm}^{-1}$  (Figure 7b) corresponding to the  $A_{1g}^{(1)}$ ,  $A_{1g}^{(2)}$ ,  $E_g^{(1)}$ ,  $A_{1g}^{(3)}$ , and  $E_g^{(2)}$  modes with apparent intensity, respectively.

The corresponding vibrations for  $A_{1g}^{(1)}$ ,  $A_{1g}^{(2)}$ ,  $E_g^{(1)}$ ,  $A_{1g}^{(3)}$ , and  $E_g^{(2)}$  modes are shown in Table 3. Furthermore, among these peaks,  $A_{1g}^{(3)}$  at  $797\text{ cm}^{-1}$  has the highest intensity and can be considered as the Raman signature of bilayer  $\text{Al}_2\text{O}_3$ .

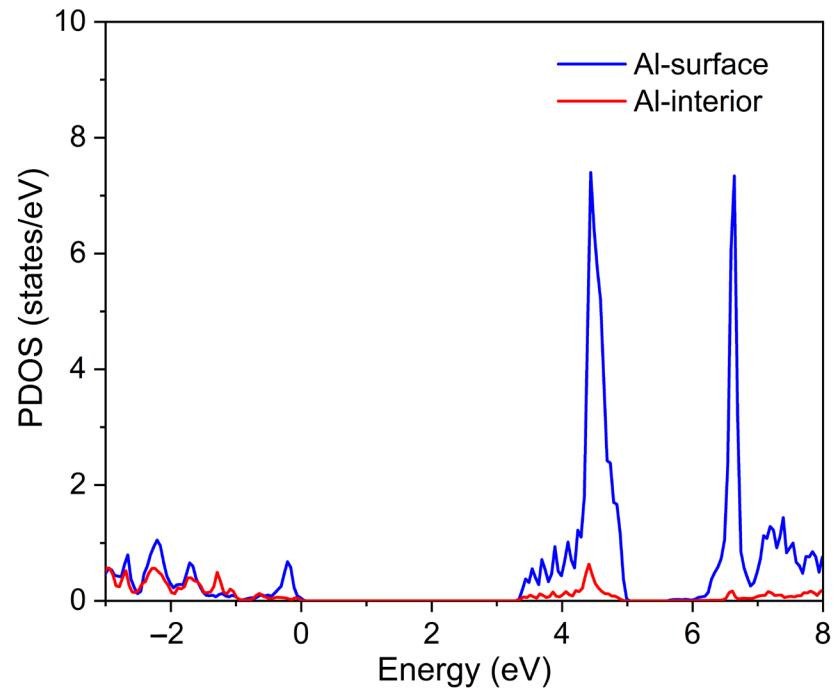


Figure 6. The partial density of states (PDOS) of Al atoms for bilayer  $\text{Al}_2\text{O}_3$ .

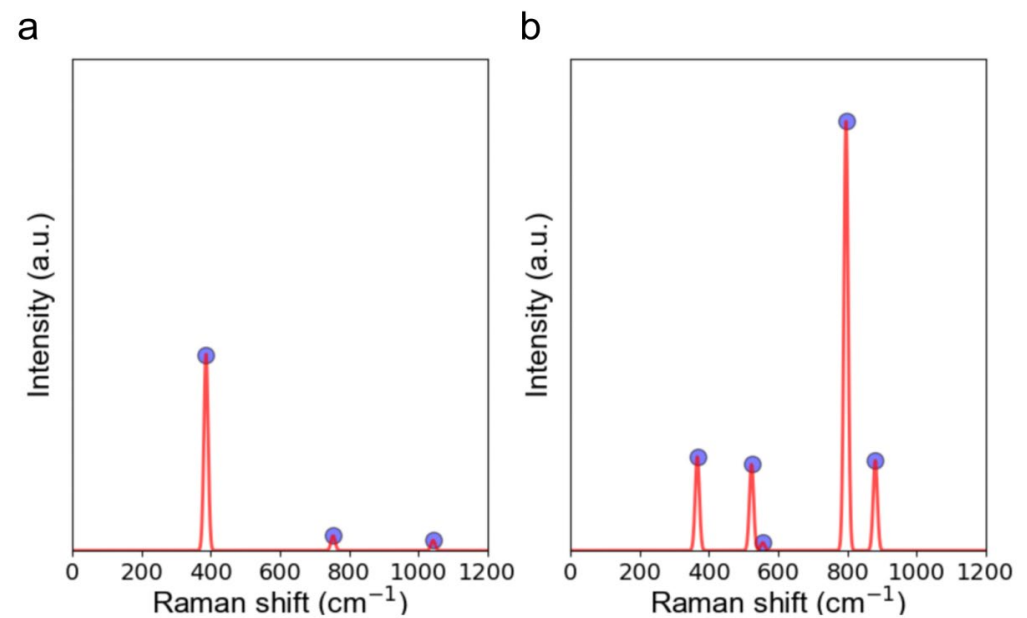


Figure 7. The calculated Raman spectra of (a) monolayer and (b) bilayer  $\text{Al}_2\text{O}_3$ .

**Table 2.** Vibrational modes for monolayer  $\text{Al}_2\text{O}_3$ .

Mode	Frequency ( $\text{cm}^{-1}$ )	Top View
$A'_1$	387	
$E'(1)$	754	
$E'(2)$	1043	

Based on the above results, which provide evidence of the stability of bilayer  $\text{Al}_2\text{O}_3$ , we can assume that the bilayer  $\text{Ga}_2\text{O}_3$  and  $\text{In}_2\text{O}_3$  are also stable because Al, Ga, and In are in the same group. The absence of negative frequencies in phonon dispersions (Figure 8a,c) demonstrates the stability of bilayer  $\text{Ga}_2\text{O}_3$  and  $\text{In}_2\text{O}_3$ . Bilayer  $\text{Ga}_2\text{O}_3$  and  $\text{In}_2\text{O}_3$  are indirect semiconductors (Figure 8b,d) with band gaps of 2.01 and 1.17 eV, respectively, which are smaller than that of bilayer  $\text{Al}_2\text{O}_3$ . The CBM of either bilayer  $\text{Ga}_2\text{O}_3$  or  $\text{In}_2\text{O}_3$  is located at the  $\Gamma$  point and the VBM at a general point along the  $K-\Gamma$  line. To obtain a variation of band structure on layer thickness, Figures 9 and 10 show the band structures of few-layer  $\text{Ga}_2\text{O}_3$  and  $\text{In}_2\text{O}_3$ , which show a similar band gap variation to that of few-layer  $\text{Al}_2\text{O}_3$ .



**Table 3.** Vibrational modes for bilayer  $\text{Al}_2\text{O}_3$ .

Mode	Frequency ( $\text{cm}^{-1}$ )	Side View
$A_{1g}^{(1)}$	367	
$A_{1g}^{(2)}$	521	
$E_g^{(1)}$	554	
$A_{1g}^{(3)}$	797	
$E_g^{(2)}$	881	

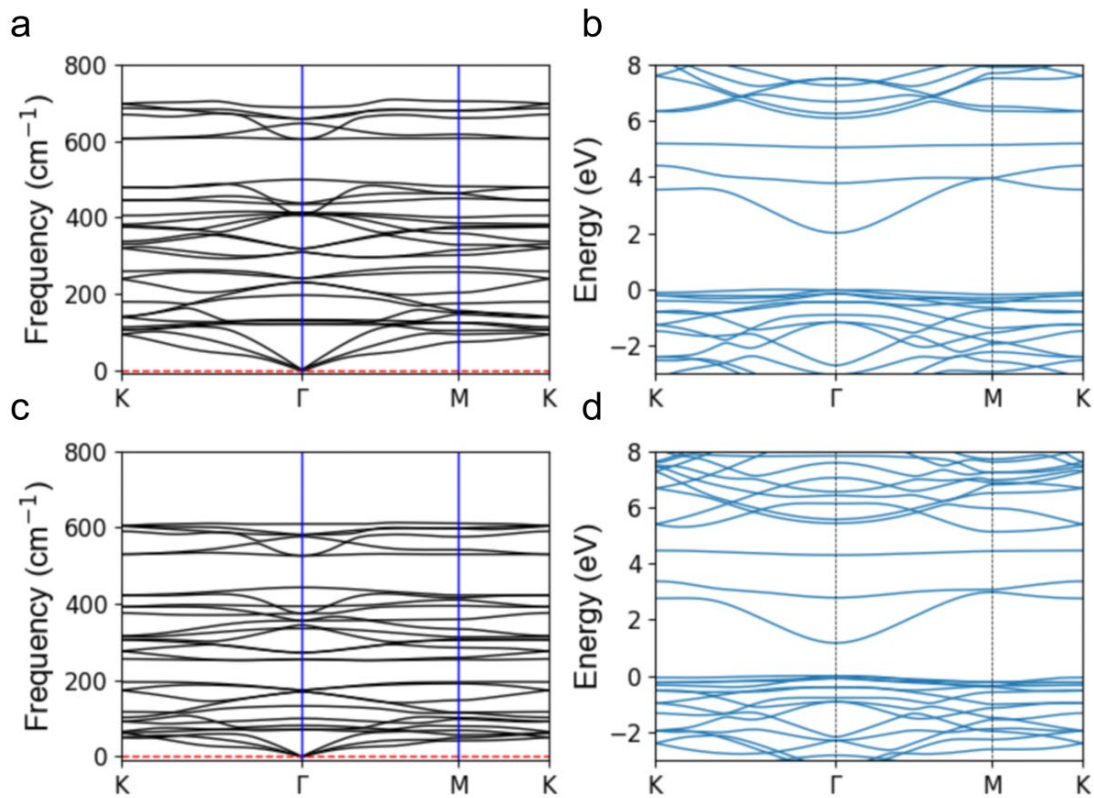


**Figure 8.** Phonon dispersions of bilayer (a)  $\text{Ga}_2\text{O}_3$  and (c)  $\text{In}_2\text{O}_3$ . Calculated electronic band structures of bilayer (b)  $\text{Ga}_2\text{O}_3$  and (d)  $\text{In}_2\text{O}_3$ . The Fermi level is set at the valence band maximum (VBM).

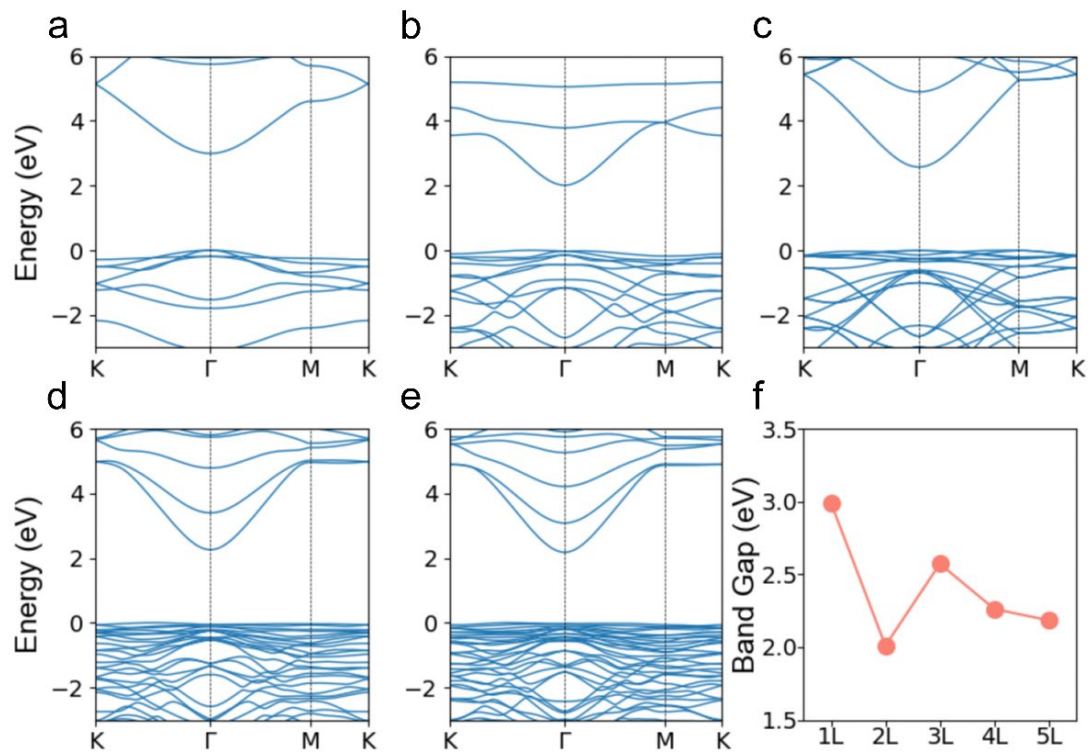


**Figure 9.** Band structures of (a) monolayer, (b) bilayer, (c) trilayer, (d) four-layer, and (e) five-layer  $\text{Ga}_2\text{O}_3$ , respectively. (f) The bandgap of few-layer  $\text{Ga}_2\text{O}_3$ .

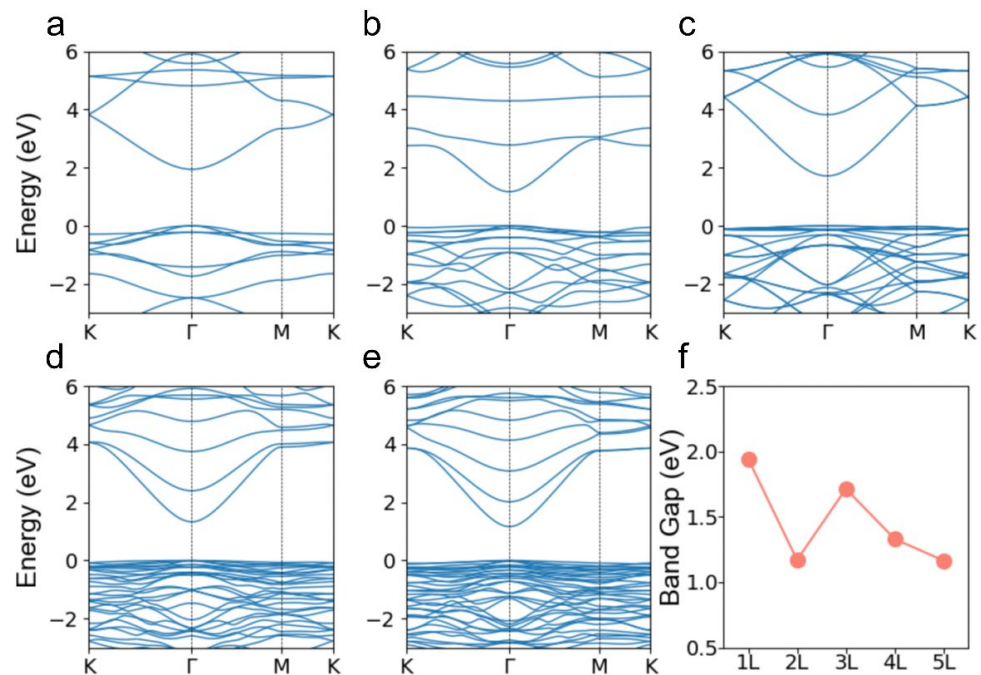


**Figure 10.** Band structures of (a) monolayer, (b) bilayer, (c) trilayer, (d) four-layer, and (e) five-layer  $\text{In}_2\text{O}_3$ , respectively. (f) The bandgap of few-layer  $\text{In}_2\text{O}_3$ .

It is also necessary to provide the Raman signature for bilayer  $\text{Ga}_2\text{O}_3$  and  $\text{In}_2\text{O}_3$ . As shown in Figure 11, the Raman spectra of bilayer  $\text{Ga}_2\text{O}_3$  and  $\text{In}_2\text{O}_3$  were calculated, which were similar to that of bilayer  $\text{Al}_2\text{O}_3$ . Bilayer  $\text{Ga}_2\text{O}_3$  and  $\text{In}_2\text{O}_3$  belong to the space group  $P\bar{3}1m$  with 2 f.u. (10 atoms) in the primitive cell. For bilayer  $\text{Ga}_2\text{O}_3$ , the peaks are centered at 196, 320, 410, 664, and 689  $\text{cm}^{-1}$  corresponding to the  $A_{1g}^{(1)}$ ,  $E_g^{(1)}$ ,  $A_{1g}^{(2)}$ ,  $E_g^{(2)}$ , and  $A_{1g}^{(3)}$  modes, respectively (Figure 11a). The corresponding vibration for  $A_{1g}^{(1)}$ ,  $E_g^{(1)}$ ,  $A_{1g}^{(2)}$ ,  $E_g^{(2)}$ , and  $A_{1g}^{(3)}$  modes are listed in Table 4. The peak centered at 689  $\text{cm}^{-1}$  ( $A_{1g}^{(3)}$ ) with strong intensity should be considered as the Raman signature of bilayer  $\text{Ga}_2\text{O}_3$ . As for bilayer  $\text{In}_2\text{O}_3$ , Figure 11b shows that there are four major peaks and two minor peaks in the Raman spectra. Six peaks centered at 133, 269, 333, 357, 580, and 607  $\text{cm}^{-1}$  correspond to the  $A_{1g}^{(1)}$ ,  $E_g^{(1)}$ ,  $A_{1g}^{(2)}$ ,  $E_g^{(2)}$ ,  $E_g^{(3)}$ , and  $A_{1g}^{(3)}$  modes, respectively. All the Raman active vibrational modes for bilayer  $\text{In}_2\text{O}_3$  can be found in Table 5. Similarly, the Raman signature of bilayer  $\text{In}_2\text{O}_3$  should be the  $A_{1g}^{(3)}$  peak, which has a pronounced intensity.

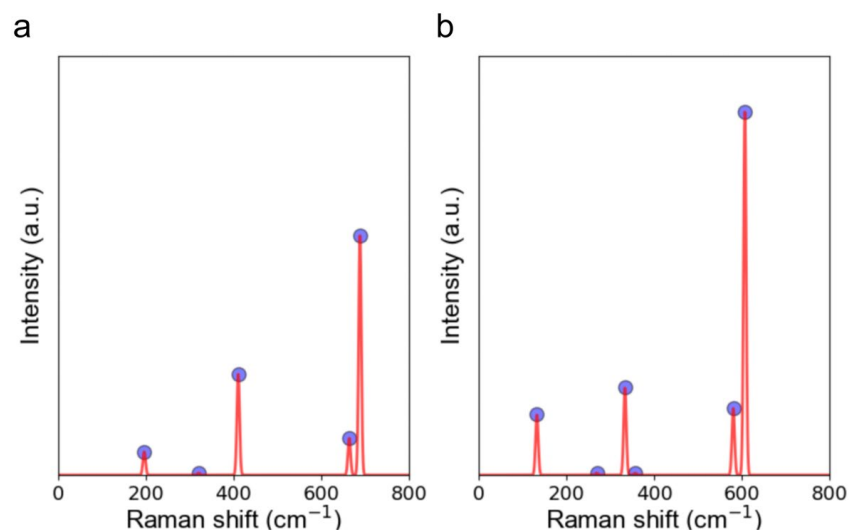


**Figure 11.** The calculated Raman spectra of bilayer (a)  $\text{Ga}_2\text{O}_3$  and (b)  $\text{In}_2\text{O}_3$ .

**Table 4.** Vibrational modes for bilayer Ga<sub>2</sub>O<sub>3</sub>.

Mode	Frequency (cm <sup>-1</sup> )	Side View
A <sub>1g</sub> <sup>(1)</sup>	196	
E <sub>g</sub> <sup>(1)</sup>	320	
A <sub>1g</sub> <sup>(2)</sup>	410	
E <sub>g</sub> <sup>(2)</sup>	664	
A <sub>1g</sub> <sup>(3)</sup>	689	

**Table 5.** Vibrational modes for bilayer  $\text{In}_2\text{O}_3$ .

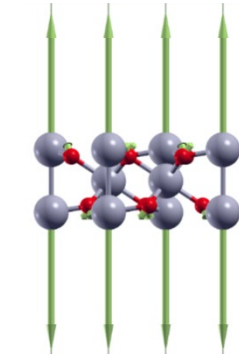
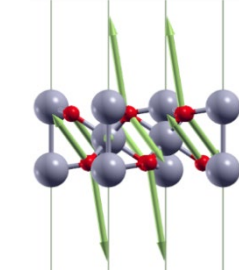
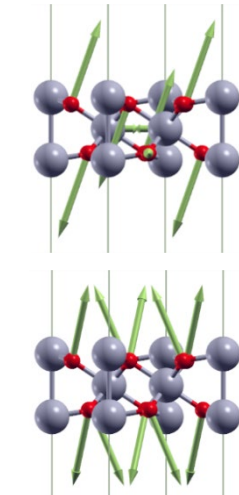
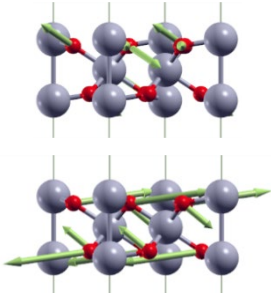
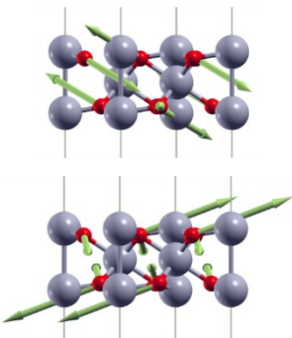
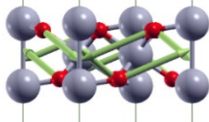
Mode	Frequency ( $\text{cm}^{-1}$ )	Side View
$A_{1g}^{(1)}$	133	
$E_g^{(1)}$	269	
$A_{1g}^{(2)}$	333	
$E_g^{(2)}$	357	

Table 5. Cont.

Mode	Frequency (cm <sup>-1</sup> )	Side View
E <sub>g</sub> <sup>(3)</sup>	580	
A <sub>1g</sub> <sup>(3)</sup>	607	

#### 4. Conclusions

In summary, using first-principles calculations based on DFT, we have investigated the structural stability and electronic properties of 2D boron group oxides. The thinnest stable Al<sub>2</sub>O<sub>3</sub> structure is a bilayer with an indirect band gap of 3.41 eV. Interestingly, we find that the band gap of Al<sub>2</sub>O<sub>3</sub> decreases with decreasing layer thickness, which is opposite to the trend seen in vdW 2D materials, such as MoS<sub>2</sub>. We attribute this to the giant surface reconstruction of Al<sub>2</sub>O<sub>3</sub>. In addition, the phonon dispersion curves and band structures show that both bilayer Ga<sub>2</sub>O<sub>3</sub> and In<sub>2</sub>O<sub>3</sub> are also stable, with band structures similar to that of bilayer Al<sub>2</sub>O<sub>3</sub>. From bilayer Al<sub>2</sub>O<sub>3</sub> to bilayer Ga<sub>2</sub>O<sub>3</sub> and In<sub>2</sub>O<sub>3</sub>, the band gap decreases with the increasing atomic radius. It is expected to synthesize few layer boron group oxides by top-down strategy, such as liquid exfoliation method. This work provides theoretical support for the discovery of non-vdW 2D boron group oxides. Because of their large band gap, non-vdW 2D boron group oxides hold potential applications in ultraviolet optoelectronics and high-power electronics.

**Author Contributions:** Y.Z. carried out the calculations. Y.C. and D.C. supervised the work. Y.Z., J.Z. and Y.C. wrote the manuscript. All authors have read and agreed to the published version of the manuscript.

**Funding:** This research was funded by the National Natural Science Foundation of China grant number 62274087.

**Data Availability Statement:** Data generated and supporting the findings of this article are available from the corresponding author upon reasonable request.

**Conflicts of Interest:** The authors declare no conflict of interest.

#### References

- Novoselov, K.S.; Geim, A.K.; Morozov, S.V.; Jiang, D.; Zhang, Y.; Dubonos, S.V.; Grigorieva, I.V.; Firsov, A.A. Electric field effect in atomically thin carbon films. *Science* **2004**, *306*, 666–669. [[CrossRef](#)] [[PubMed](#)]
- Chhowalla, M.; Shin, H.S.; Eda, G.; Li, L.J.; Loh, K.P.; Zhang, H. The chemistry of two-dimensional layered transition metal dichalcogenide nanosheets. *Nat. Chem.* **2013**, *5*, 263–275. [[CrossRef](#)] [[PubMed](#)]
- Huang, X.; Zeng, Z.; Zhang, H. Metal dichalcogenide nanosheets: Preparation, properties and applications. *Chem. Soc. Rev.* **2013**, *42*, 1934–1946. [[CrossRef](#)] [[PubMed](#)]
- Xu, M.; Liang, T.; Shi, M.; Chen, H. Graphene-like two-dimensional materials. *Chem. Rev.* **2013**, *113*, 3766–3798. [[CrossRef](#)] [[PubMed](#)]
- Jiang, J.; Guo, Y.; Weng, X.; Long, F.; Xin, Y.; Lu, Y.; Ye, Z.; Ruan, S.; Zeng, Y.-J. A tailorable polarity-flipping response in self-powered, flexible Sb<sub>2</sub>Se<sub>3</sub>/ZnO bilayer photodetectors. *J. Mater. Chem. C* **2021**, *9*, 4978–4988. [[CrossRef](#)]

6. Dral, A.P.; ten Elshof, J.E. 2D metal oxide nanoflakes for sensing applications: Review and perspective. *Sens. Actuators B Chem.* **2018**, *272*, 369–392. [[CrossRef](#)]
7. Huang, S.; Long, Y.; Ruan, S.; Zeng, Y.-J. Enhanced photocatalytic CO<sub>2</sub> reduction in defect-engineered Z-scheme WO<sub>3-x</sub>/g-C<sub>3</sub>N<sub>4</sub> heterostructures. *ACS Omega* **2019**, *4*, 15593–15599. [[CrossRef](#)]
8. Jiao, S.; Fu, X.; Zhang, L.; Zeng, Y.-J.; Huang, H. Point-defect-optimized electron distribution for enhanced electrocatalysis: Towards the perfection of the imperfections. *Nano Today* **2020**, *31*, 100833. [[CrossRef](#)]
9. Cakici, M.; Reddy, K.R.; Alonso-Marroquin, F. Advanced electrochemical energy storage supercapacitors based on the flexible carbon fiber fabric-coated with uniform coral-like MnO<sub>2</sub> structured electrodes. *Chem. Eng. J.* **2017**, *309*, 151–158. [[CrossRef](#)]
10. Al-Hardan, N.H.; Abdullah, M.J.; Ahmed, N.M.; Yam, F.K.; Aziz, A.A. UV photodetector behavior of 2D ZnO plates prepared by electrochemical deposition. *Superlattices Microstruct.* **2012**, *51*, 765–771. [[CrossRef](#)]
11. Yin, Z.; Xu, K.; Jiang, S.; Luo, D.; Chen, R.; Xu, C.; Shum, P.; Liu, Y.J. Recent progress on two-dimensional layered materials for surface enhanced Raman spectroscopy and their applications. *Mater. Today Phys.* **2021**, *18*, 100378. [[CrossRef](#)]
12. Singh, A.K.; Hennig, R.G. Computational prediction of two-dimensional group-IV mono-chalcogenides. *Appl. Phys. Lett.* **2014**, *105*, 042103. [[CrossRef](#)]
13. Wang, Y.; Zhang, Q.; Shen, Q.; Cheng, Y.; Schwingenschlogl, U.; Huang, W. Lead monoxide: A two-dimensional ferromagnetic semiconductor induced by hole-doping. *J. Mater. Chem. C* **2017**, *5*, 4520–4525. [[CrossRef](#)]
14. Daeneke, T.; Atkin, P.; Orrell-Trigg, R.; Zavabeti, A.; Ahmed, T.; Walia, S.; Liu, M.; Tachibana, Y.; Javid, M.; Greentree, A.D.; et al. Wafer-scale synthesis of semiconducting SnO monolayers from interfacial oxide layers of metallic liquid tin. *ACS Nano* **2017**, *11*, 10974–10983. [[CrossRef](#)] [[PubMed](#)]
15. Yan, B.; Zhou, P.; Xu, Q.; Zhou, X.; Xu, D.; Zhu, J. Engineering disorder into exotic electronic 2D TiO<sub>2</sub> nanosheets for enhanced photocatalytic performance. *RSC Adv.* **2016**, *6*, 6133–6137. [[CrossRef](#)]
16. Tao, J.; Luttrell, T.; Batzill, M. A two-dimensional phase of TiO<sub>2</sub> with a reduced bandgap. *Nat. Chem.* **2011**, *3*, 296–300. [[CrossRef](#)]
17. Addou, R.; Dahal, A.; Batzill, M. Growth of a two-dimensional dielectric monolayer on quasi-freestanding graphene. *Nat. Nanotechnol.* **2013**, *8*, 41–45. [[CrossRef](#)]
18. Matsuzaki, K.; Hosono, H.; Susaki, T. Layer-by-layer epitaxial growth of polar MgO(111) thin films. *Phys. Rev. B* **2010**, *82*, 033408. [[CrossRef](#)]
19. Sun, Z.; Liao, T.; Dou, Y.; Hwang, S.M.; Park, M.-S.; Jiang, L.; Kim, J.H.; Dou, S.X. Generalized self-assembly of scalable two-dimensional transition metal oxide nanosheets. *Nat. Commun.* **2014**, *5*, 3813. [[CrossRef](#)]
20. Yang, M.; Ye, Z.; Iqbal, M.A.; Liang, H.; Zeng, Y.-J. Progress on two-dimensional binary oxide materials. *Nanoscale* **2022**, *14*, 9576–9608. [[CrossRef](#)]
21. Lee, H.-Y.; Liu, J.-T.; Lee, C.-T. Modulated Al<sub>2</sub>O<sub>3</sub>-Alloyed Ga<sub>2</sub>O<sub>3</sub> Materials and Deep Ultraviolet Photodetectors. *IEEE Photon. Technol. Lett.* **2018**, *30*, 549–552. [[CrossRef](#)]
22. Liu, J.W.; Liao, M.Y.; Imura, M.; Banal, R.G.; Koide, Y. Deposition of TiO<sub>2</sub>/Al<sub>2</sub>O<sub>3</sub> bilayer on hydrogenated diamond for electronic devices: Capacitors, field-effect transistors, and logic inverters. *J. Appl. Phys.* **2017**, *121*, 224502. [[CrossRef](#)]
23. Chang, C.-W.; Kuo, C.-P. Evaluation of surface roughness in laser-assisted machining of aluminum oxide ceramics with Taguchi method. *Int. J. Mach. Tools Manuf.* **2007**, *47*, 141–147. [[CrossRef](#)]
24. Komine, F.; Tomic, M.; Gerds, T.; Strub, J.R. Influence of different adhesive resin cements on the fracture strength of aluminum oxide ceramic posterior crowns. *J. Prosthet. Dent.* **2004**, *92*, 359–364. [[CrossRef](#)] [[PubMed](#)]
25. Vekinis, G.; Ashby, M.F.; Beaumont, P.W.R. R-curve behaviour of Al<sub>2</sub>O<sub>3</sub> ceramics. *Acta Metall. Mater.* **1990**, *38*, 1151–1162. [[CrossRef](#)]
26. Huang, Z.; Zhou, A.; Wu, J.; Chen, Y.; Lan, X.; Bai, H.; Li, L. Bottom-up preparation of ultrathin 2D aluminum oxide nanosheets by duplicating graphene oxide. *Adv. Mater.* **2016**, *28*, 1703–1708. [[CrossRef](#)]
27. Ozyurt, A.K.; Molavali, D.; Sahin, H. Stable single layer structures of aluminum oxide: Vibrational and electronic characterization of magnetic phases. *Comput. Mater. Sci.* **2022**, *214*, 111745. [[CrossRef](#)]
28. Hasan, S.R.; Abbas, Z.; Khan, M.S. The Al<sub>2</sub>O<sub>3</sub>-monolayer sensitivity towards NH<sub>3</sub> and PH<sub>3</sub> molecule: A DFT Study. *J. Water Environ. Nanotechnol.* **2023**, *8*, 31–40.
29. Song, T.T.; Yang, M.; Chai, J.W.; Callsen, M.; Zhou, J.; Yang, T.; Zhang, Z.; Pan, J.S.; Chi, D.Z.; Feng, Y.P.; et al. The stability of aluminium oxide monolayer and its interface with two-dimensional materials. *Sci. Rep.* **2016**, *6*, 29221. [[CrossRef](#)]
30. Chen, X.; Ren, F.; Gu, S.; Ye, J. Review of gallium-oxide-based solar-blind ultraviolet photodetectors. *Photonics Res.* **2019**, *7*, 381–415. [[CrossRef](#)]
31. Dong, H.; Long, S.; Sun, H.; Zhao, X.; He, Q.; Qin, Y.; Jian, G.; Zhou, X.; Yu, Y.; Guo, W.; et al. Fast switching beta-Ga<sub>2</sub>O<sub>3</sub> power MOSFET with a trench-gate Structure. *IEEE Electron Device Lett.* **2019**, *40*, 1385–1388. [[CrossRef](#)]
32. Green, A.J.; Chabak, K.D.; Baldini, M.; Moser, N.; Gilbert, R.; Fitch, R.C., Jr.; Wagner, G.; Galazka, Z.; McCandless, J.; Crespo, A.; et al. Beta-Ga<sub>2</sub>O<sub>3</sub> MOSFETs for radio frequency operation. *IEEE Electron Device Lett.* **2017**, *38*, 790–793. [[CrossRef](#)]
33. Mukhopadhyay, P.; Schoenfeld, W.V. High responsivity tin gallium oxide Schottky ultraviolet photodetectors. *J. Vac. Sci. Technol. A* **2020**, *38*, 013403. [[CrossRef](#)]
34. Zhang, D.; Du, Z.; Ma, M.; Zheng, W.; Liu, S.; Huang, F. Enhanced performance of solar-blind ultraviolet photodetector based on Mg-doped amorphous gallium oxide film. *Vacuum* **2019**, *159*, 204–208. [[CrossRef](#)]

35. Manificier, J.C.; Szepessy, L. Efficient sprayed  $\text{In}_2\text{O}_3:\text{Sn}$  n-type silicon heterojunction solar cell. *Appl. Phys. Lett.* **1977**, *31*, 459–462. [[CrossRef](#)]
36. Hamberg, I.; Granqvist, C.G. Evaporated Sn-doped  $\text{In}_2\text{O}_3$  films: Basic optical properties and applications to energy-efficient windows. *J. Appl. Phys.* **1986**, *60*, R123–R159. [[CrossRef](#)]
37. Lee, J.S.; Kwack, Y.J.; Choi, W.S. Inkjet-printed  $\text{In}_2\text{O}_3$  thin-film transistor below 200 degrees C. *ACS Appl. Mater. Interfaces* **2013**, *5*, 11578–11583. [[CrossRef](#)]
38. Von Wenckstern, H.; Splith, D.; Schmidt, F.; Grundmann, M.; Bierwagen, O.; Speck, J.S. Schottky contacts to  $\text{In}_2\text{O}_3$ . *APL Mater.* **2014**, *2*, 046104. [[CrossRef](#)]
39. Lee, D.; Seo, J. Graphene growth on sapphire via palladium silicidation. *Appl. Surf. Sci.* **2019**, *492*, 23–26. [[CrossRef](#)]
40. Liu, H.; Chi, D. Dispersive growth and laser-induced rippling of large-area singlelayer  $\text{MoS}_2$  nanosheets by CVD on c-plane sapphire substrate. *Sci. Rep.* **2015**, *5*, 11756. [[CrossRef](#)]
41. Thakur, D.; Sharma, M.; Balakrishnan, V.; Vaish, R. Reusable piezocatalytic water disinfection activity of CVD-grown few-layer  $\text{WS}_2$  on sapphire substrate. *Environ. Sci. Nano* **2022**, *9*, 805–814. [[CrossRef](#)]
42. Yang, W.; Mu, Y.; Chen, X.; Jin, N.; Song, J.; Chen, J.; Dong, L.; Liu, C.; Xuan, W.; Zhou, C.; et al. CVD growth of large-area monolayer  $\text{WS}_2$  film on sapphire through tuning substrate environment and its application for high-sensitive strain sensor. *Nanoscale Res. Lett.* **2023**, *18*, 13. [[CrossRef](#)] [[PubMed](#)]
43. Balan, A.P.; Radhakrishnan, S.; Woellner, C.F.; Sinha, S.K.; Deng, L.; de los Reyes, C.; Rao, B.M.; Paulose, M.; Neupane, R.; Apte, A.; et al. Exfoliation of a non-van der Waals material from iron ore hematite. *Nat. Nanotechnol.* **2018**, *13*, 602–609. [[CrossRef](#)] [[PubMed](#)]
44. Giannozzi, P.; Andreussi, O.; Brumme, T.; Bunau, O.; Nardelli, M.B.; Calandra, M.; Car, R.; Cavazzoni, C.; Ceresoli, D.; Cococcioni, M.; et al. Advanced capabilities for materials modelling with QUANTUM ESPRESSO. *J. Phys. Condens. Matter* **2017**, *29*, 465901. [[CrossRef](#)]
45. Giannozzi, P.; Baroni, S.; Bonini, N.; Calandra, M.; Car, R.; Cavazzoni, C.; Ceresoli, D.; Chiarotti, G.L.; Cococcioni, M.; Dabo, I.; et al. QUANTUM ESPRESSO: A modular and open-source software project for quantum simulations of materials. *J. Phys. Condens. Matter* **2009**, *21*, 395502. [[CrossRef](#)]
46. Perdew, J.P.; Burke, K.; Ernzerhof, M. Generalized gradient approximation made simple. *Phys. Rev. Lett.* **1996**, *77*, 3865–3868. [[CrossRef](#)]
47. Monkhorst, H.J.; Pack, J.D. Special points for Brillouin-zone integrations. *Phys. Rev. B* **1976**, *13*, 5188–5192. [[CrossRef](#)]
48. Baroni, S.; de Gironcoli, S.; Dal Corso, A.; Giannozzi, P. Phonons and related crystal properties from density-functional perturbation theory. *Rev. Mod. Phys.* **2001**, *73*, 515–562. [[CrossRef](#)]
49. Santos, R.C.R.; Longhinotti, E.; Freire, V.N.; Reimberg, R.B.; Caetano, E.W.S. Elucidating the high-k insulator  $\alpha\text{-Al}_2\text{O}_3$  direct/indirect energy band gap type through density functional theory computations. *Chem. Phys. Lett.* **2015**, *637*, 172–176. [[CrossRef](#)]
50. Pham, A.; Assadi, M.H.N.; Yu, A.B.; Li, S. Critical role of Fock exchange in characterizing dopant geometry and magnetic interaction in magnetic semiconductors. *Phys. Rev. B* **2014**, *89*, 155110. [[CrossRef](#)]
51. Sousa, S.F.; Fernandes, P.A.; Ramos, M.J. General performance of density functionals. *J. Phys. Chem. A* **2007**, *111*, 10439–10452. [[CrossRef](#)] [[PubMed](#)]

**Disclaimer/Publisher’s Note:** The statements, opinions and data contained in all publications are solely those of the individual author(s) and contributor(s) and not of MDPI and/or the editor(s). MDPI and/or the editor(s) disclaim responsibility for any injury to people or property resulting from any ideas, methods, instructions or products referred to in the content.